The growth of protrusions at the boundary of a recrystallized grain

M.A. Martorano [a,*], M.A. Fortes [b], A.F. Padilha [a]

[a] *Departamento de Engenharia, Metalúrgica e de Materiais, Universidade de São Paulo, Av. Prof. Mello Moraes, 2463, São Paulo-SP 05508-900, Brazil*
[b] *Departamento de Engenharia de Materiais, Instituto Superior Técnico, Av. Rovisco Pais, 1049-001 Lisboa, Portugal*

Abstract

The growth of mesoscopic protrusions at originally straight and circular boundaries of two-dimensional recrystallized grains is simulated by numerical integration of a modified form of the classic kinetic equation for boundary migration. The modified equation relates the boundary velocity in a fixed direction to the boundary curvature and to a non-uniform excess strain energy density in the matrix due to dislocation walls. Calculations are made for an array of equispaced dislocation walls perpendicular to the original boundaries, which migrate, changing their shape, while absorbing the dislocation walls. The strain field of the walls is represented by a sinusoidal function. The time evolution of the boundary shape is calculated for unbounded dislocation walls and for a simplified network of staggered rows of dislocation walls. Steady and scaled regimes of the boundary shape may be reached, which are characterized in detail.
© 2006 Acta Materialia Inc. Published by Elsevier Ltd. All rights reserved.

Keywords: Grain boundary migration; Recrystallization kinetics; Modelling

1. Introduction

In the recrystallization of work-hardened metals and alloys, the boundaries of the recrystallized grains migrate under the combined effects of boundary energy (boundary curvature) and of the excess strain energy density in the surrounding matrix [1–3]. A recrystallized grain has a low density of dislocations compared to that in the matrix, where the dislocations are frequently arranged in walls, particularly at low-angle boundaries (or sub-boundaries) that formed in the recovery stage preceding recrystallization. As the recrystallized grain boundary advances into the matrix it absorbs the dislocations ahead and maintains the strain energy density difference that compensates for the increase in the boundary area. Since the distribution of dislocations in the matrix is highly non-uniform, the moving boundary develops protrusions (also termed serrations or undulations) into the matrix. As examples, Kassner and McMahon [4] and Drury and Humphreys

[5] indicated that protrusions develop at the junctions between subgrain boundaries and high-angle grain boundaries during recrystallization of Al. Mesoscopic protrusions of amplitudes between 0.5 and 50 μm have been observed in the recrystallization (both static and dynamic) of pure metals and solid solutions [6–10] and also in alloys containing precipitates [11–14]. In the latter, there is a correlation between the occurrence of serrations and the morphology and mechanisms of growth of the precipitates. Recently, the in situ growth of recrystallized grains in the bulk of commercially pure Al was observed with a new three-dimensional X-ray diffraction microscope [15]. A very heterogeneous growth pattern was observed, with irregular growth protrusions of different amplitudes and widths.

The purpose of this paper is to model the formation and time evolution of protrusions in two-dimensional (2D) grain boundaries during their migration. To the authors' knowledge, the evolution of such protrusions has never been modelled before. For initially straight and circular boundaries, the boundary shape as a function of time is obtained by integration of an appropriate form of the kinetic equation derived in the present work.

---

* Corresponding author. Tel.: +55 11 3091 6032; fax: +55 11 3091 5243.
  E-mail addresses: martoran@usp.br (M.A. Martorano), l.marcelino@ist.utl.pt (M.A. Fortes), padilha@usp.br (A.F. Padilha).
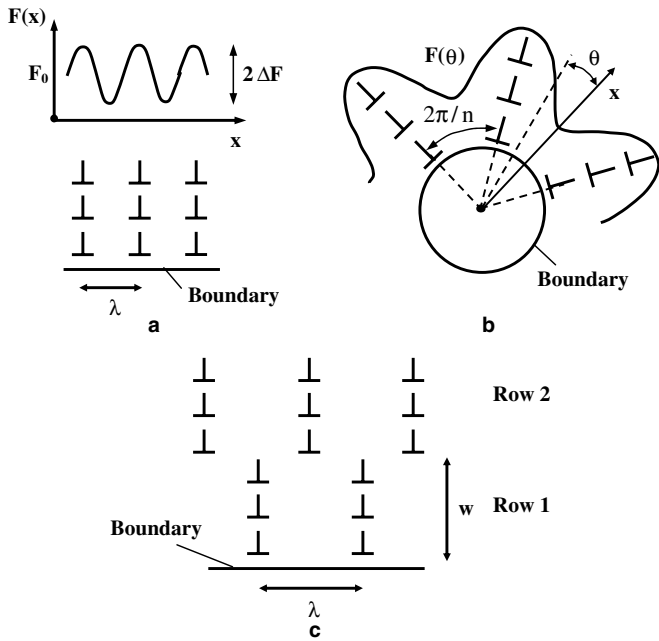
Fig. 1. Sinusoidal bulk pressure for unbounded dislocation walls contacting an initially: (a) flat boundary and (b) circular boundary. (c) A simplified network of dislocation walls at an originally flat boundary.

Two types of arrangement of the dislocation walls around the recrystallized grain are considered. In one, shown in Fig. 1(a) and (b), the walls are identical, unbounded, equally spaced, and perpendicular to the straight or circular boundary. For initially straight boundaries, a more realistic arrangement of the dislocation walls in the matrix (Fig. 1(c)) is also used as a simplified model of a network of walls.

2. The kinetic equation

The kinetic equation of 2D boundary migration under the effects of boundary energy and a bulk energy density difference F is [16,17]

$$v_n = M\left(\frac{\sigma}{R} + F\right) \tag{1}$$

where v_n is the local boundary velocity along its normal $\boldsymbol{n}$ directed to the grain of largest bulk strain energy; R is the local radius of curvature (positive or negative); σ is the boundary energy per unit area; and M is the boundary mobility. The strain energy density difference F, i.e. the excess energy density of the matrix in relation to the recrystallized grain, varies along the boundary and has 'peaks' at the intersections with dislocation walls, decaying to small values ('valleys') halfway between them. This excess energy density F (or driving pressure) will be represented by a sinusoidal function of a space variable. Because the strain field of dislocation walls is short-ranged, a more realistic description of F would be a stepped function with narrow periodic peaks, but this is more difficult to handle analytically.

For an originally straight boundary, rectangular coordinates x and y were used, with the boundary initially at $y = 0$, and the recrystallized grain at $y < 0$ (Fig. 1(a)). For equispaced unbounded dislocation walls (Fig. 1(a)), the driving pressure F is

$$F = F_0 + \Delta F \sin\frac{2\pi x}{\lambda} \tag{2}$$

where F_0 and ΔF are the mean value and amplitude of F, respectively, and the wavelength λ equals the separation distance between dislocation walls. The boundary shape is defined by $y = y(x, t)$ where t is time.

For an initially circular boundary of radius r_0 enclosing the recrystallized grain, polar coordinates were used, with origin at the centre of the boundary (Fig. 1(b)). For equispaced unbounded dislocation walls (Fig. 1(b)), the driving pressure F is

$$F = F_0 + \Delta F \sin(n\theta) \tag{3}$$

where n ($n > 1$) is an integer. In this case, the boundary shape is given by $r = r(\theta, t)$, where θ is the angular coordinate, defined relative to an arbitrary radial direction x (Fig. 1(b)).

For the initially straight boundary, the network of dislocation walls referred to above is characterized by the inter-wall separation λ in each row (Fig. 1(c)) and by the width w of one row. The walls in successive rows are translated by $\lambda/2$. The driving pressure F acting on a boundary traversing rows 1, 3, 5, ... of dislocation walls (row 1 is adjacent to the boundary) is given by Eq. (2). For a boundary traversing rows 2, 4, 6, ... the driving pressure is

$$F = F_0 + \Delta F \sin\frac{2\pi\left(x + \frac{\lambda}{2}\right)}{\lambda} \tag{4}$$

The peaks and valleys of F are thus abruptly translated by $\lambda/2$ in successive rows. In reality, there will be other dislocation walls connecting those in successive rows (e.g. a hexagonal network), but they will not be considered.

While the driving pressure σ/R in Eq. (1) pushes the boundary to its centre of curvature, the bulk driving pressure F pushes it into the matrix. This requires that $F_0 \geqslant \Delta F > 0$. The sign of the radius of curvature R of the boundary is positive if its centre of curvature is in the matrix and vice versa.

To determine the boundary evolution, it is sufficient to calculate the velocity component along the y or r directions in either boundary shapes (straight or circular). This strategy, described below, is introduced for the first time in the present paper and greatly simplifies the numerical solution to the kinetic equation. In the case of the initially straight boundary in the $x - y$ plane, the boundary curve is assumed to be a function of the x coordinate only. Therefore, it can be parametrically represented by $\zeta = x\boldsymbol{e}_x + y(x,t)\boldsymbol{e}_y$, where t is time and $\boldsymbol{e}_x$ and $\boldsymbol{e}_y$ are unit vectors. The boundary velocity is simply

$$\boldsymbol{V} = \frac{\partial \zeta}{\partial t} = \frac{\partial y}{\partial t}\boldsymbol{e}_y \tag{5}$$

Since the normal vector to the boundary is $\boldsymbol{n} = (1 + \dot{y}^2)^{-1/2}(-\dot{y}\boldsymbol{e}_x + \boldsymbol{e}_y)$, where $\dot{y} = \partial y/\partial x$, the normal boundary velocity v_n is calculated by

$$\boldsymbol{V}.\boldsymbol{n} = v_n = \frac{\partial y}{\partial t}(1 + \dot{y}^2)^{-1/2} \qquad (6)$$

Finally, Eq. (6) is substituted in Eq. (1), in which the radius of curvature is calculated by the well-known relation $R = (1 + \dot{y}^2)^{3/2}/\ddot{y}$ (e.g. Ref. [18]), yielding, for F given by Eq. (2)

$$\frac{\partial y^*}{\partial t^*} = \ddot{y}^*(1 + \dot{y}^{*2})^{-1} + [F_0^* + \Delta F^* \sin(2\pi x^*)](1 + \dot{y}^{*2})^{1/2} \qquad (7)$$

where we introduced reduced dimensionless quantities $x^* = x/\lambda$; $y^* = y/\lambda$; $t^* = M\sigma t/\lambda^2$; $F^* = \lambda F/\sigma$; and $\Delta F^* = \lambda\Delta F/\sigma$. Similarly, for an initially circular boundary, the following kinetic equation yielding the radial velocity, $\partial r^*/\partial t^*$, can be derived from Eqs. (1) and (3):

$$\frac{\partial r^*}{\partial t^*} = \left(\ddot{r}^* - \frac{2\dot{r}^*}{r^*} - r^*\right)(r^{*2} + \dot{r}^{*2})^{-1}$$
$$+ [F_0^* + \Delta F^* \sin(n\theta)]\frac{(r^{*2} + \dot{r}^{*2})^{1/2}}{r^*} \qquad (8)$$

where $\dot{r}^* = \partial r^*/\partial\theta$. The reduced quantities in this equation are similar to those defined above, but r_0 (the initial radius of the boundary) replaces λ (e.g. $r^* = r/r_0$; $F_0^* = r_0 F_0/\sigma$). The first term on the right-hand side of Eq. (8) is the curvature, $1/R$, of a curve $r(\theta)$ in polar coordinates (e.g. Ref. [18]).

Typical values of the average stored energy of cold work F_0 for common metals range between 2×10^6 and 10×10^6 J m^{-3} depending on the metal and the degree of deformation, while σ (the energy of a high-angle boundary) is typically in the interval 0.2–0.5 J m^{-2}. For interspacings λ between dislocation walls in the interval 1–50 µm, the estimated extreme values of $F_0^* = \lambda F_0/\sigma$ are 5 and 250. For a growing recrystallized grain, the reduced amplitude ΔF^* ranges between 0 and F_0^* ($\Delta F^*/F_0^*$ in the interval $[0,1]$), as pointed out above.

3. Solution of the kinetic equations

In both cases under discussion the evolving boundaries have the period of the driving force F. Hence, the implicit formulation of the finite difference method [19] was used to solve Eqs. (7) and (8) in one period, with initial conditions $y^*(x^*, 0) = 0$ and $r^*(\theta, 0) = 1$, respectively. The first and second partial derivatives in relation to the spatial coordinates were discretized by central differences. After discretizing the equations, the resulting non-linear system of algebraic equations was solved iteratively by the following steps: (1) the system was transformed into a tridiagonal linear system by keeping some terms constant at their latest iteration values; (2) the linearized system was solved by the Thomas algorithm [19]; and (3) all terms that were kept constant in the previous steps were updated, and steps (1) and (2) were repeated. This iterative process stopped when

the maximum relative difference between the values of the grain boundary position (i.e. y^* or r^*) in two consecutive iterations was lower than 10^{-7}. The time step for the marching down process of the numerical method was adjusted to be the largest value that still guaranteed convergence of the iterative process. The adopted time step values were always smaller than 10^{-5}. After examining the numerical solution for meshes of an increasingly large number of nodes, a mesh of 801 equally spaced nodes was found to yield a mesh-independent solution and was, therefore, adopted.

The time evolution of the boundaries obtained by this numerical solution was compared with those calculated with an alternative method recently developed by the authors [20], showing excellent agreement. This alternative method is more robust, being capable of tracking the migration of several types of 2D boundaries, but needs a 2D mesh of cells to work. Solutions to Eqs. (7) and (8), however, can be readily obtained using standard numerical methods and a one-dimensional mesh of nodes. Nevertheless, they are limited to model the migration of boundaries that can be described as a function of only one of the coordinates.

4. Results and discussion

The results for the initially flat (straight) boundary moving through unbounded dislocation walls and through a network of walls are first described in Sections 4.1 and 4.2. Section 4.3 deals with the case of an initially circular boundary and Section 4.4 presents an attempt to compare some of the results with experiments reported in the literature. A comparison with other published theoretical results was not possible, because, to the authors' knowledge, these are not available in the literature.

4.1. Initially straight boundaries: unbounded dislocation walls

The evolution of an initially straight boundary subjected to a time-independent bulk driving pressure F given by Eq. (2) is shown in Fig. 2(a) for $F_0^* = 5$ and $\Delta F^*/F_0^* = 0.5$. Periodic protrusions develop, which are similar to those experimentally observed in cross-sections of three-dimensional recrystallized grains. At sufficiently long times ($t^* \gtrsim 0.07$ in Fig. 2(a)), the boundary shape remains invariant, i.e. reaches steady state: the undulated boundary simply translates in the y-direction, with a uniform and time-invariant velocity $\partial y^*/\partial t^*$. In the numerical calculations, the steady-state amplitude was considered as the one prevailing when the change in protrusion amplitude during one time step became comparable to the round-off errors of the calculations. The evolution of the amplitude to this steady-state value is shown in Fig. 3 (dashed curves) for two pairs of values of F_0^* and $\Delta F^*/F_0^*$. Note that $\Delta F^*/F_0^*$ is a measure of the sharpness of the driving pressure near the peaks.
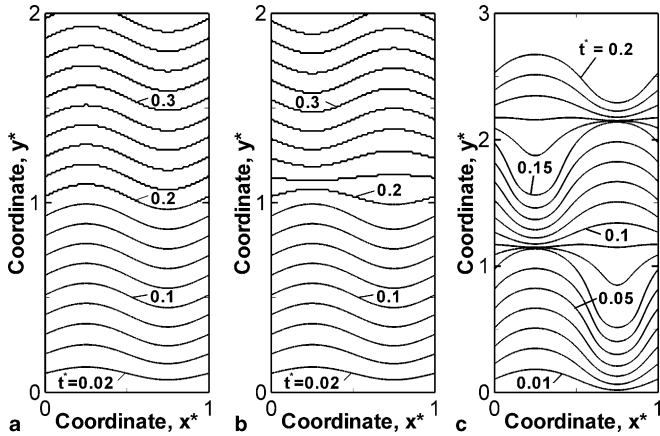
Fig. 2. Time evolution of an initially straight boundary in a fixed reference frame for: (a) unbounded dislocation walls with $F_0^* = 5$ and $\Delta F^*/F_0^* = 0.5$; (b) dislocation wall network with $F_0^* = 5$ and $\Delta F^*/F_0^* = 0.5$ ($y_S^* < 1$); and (c) dislocation wall network with $F_0^* = 10$ and $\Delta F^*/F_0^* = 1$ ($y_S^* > 1$). Time intervals are 0.02 for (a) and (b), and 0.01 for (c).
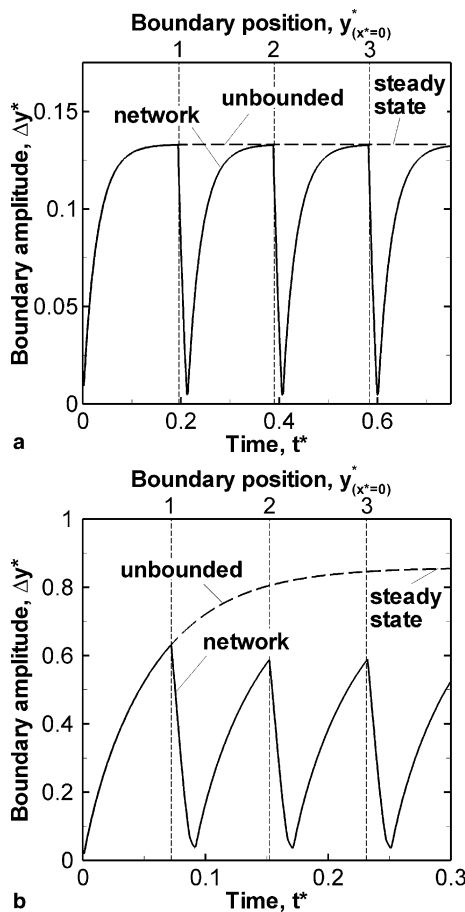

Fig. 3. Total amplitude of boundary protrusions grown at an initially straight boundary as a function of time and position, for unbounded walls and network: (a) $F_0^* = 5$, $\Delta F^*/F_0^* = 0.5$ ($y_S^* < 1$); (b) $F_0^* = 10$, $\Delta F^*/F_0^* = 1$ ($y_S^* > 1$). In (a) the boundary reaches steady state within a row of dislocation walls, while in (b) steady state is not reached.

Fig. 4 shows the steady-state boundary shapes (plotted in a frame moving with the boundary) for two values of $\Delta F^*/F_0^*$ and various values of F_0^*. As F_0^* or ΔF^* increases,

the steady-state shapes become increasingly asymmetric: valleys are deeper than peaks, with increasing curvature κ_v at their bottoms. The height and curvature of the peaks κ_p are always smaller than those of the valleys. The difference in curvature $\Delta\kappa = |\kappa_v| - |\kappa_p|$ can be obtained from Eq. (7) by setting $\dot{y} = 0$. The result is $\Delta\kappa^* = 2\Delta F^*$, where $\kappa^* = \kappa\lambda$, indicating that larger driving force amplitudes result in less symmetrical shapes.

The plots of Fig. 5 show the effects of F_0^* and ΔF^* on: the amplitude of the protrusions Δy^* in the steady state, defined as the separation between extreme points in the y direction (Fig. 5(a)); the steady-state (time-invariant) boundary velocity, $V_S^* = (\partial y^*/\partial t)_S$ (Fig. 5(b)); and the reduced distance y_S^* that the boundary moved to reach the steady state (Fig. 5(c)). This distance was defined as the boundary displacement at $x^* = 0$ until the protrusion amplitude reached 90% of the final steady-state amplitude. This distance is more easily determined than the exact one to reach the steady-state shape, which is strongly affected by round-off errors.

The amplitude of the protrusions at fixed F_0^* (Fig. 5(a)) increases both with ΔF^* (with $\Delta F^* \leqslant F_0^*$) and with $\Delta F^*/F_0^*$.
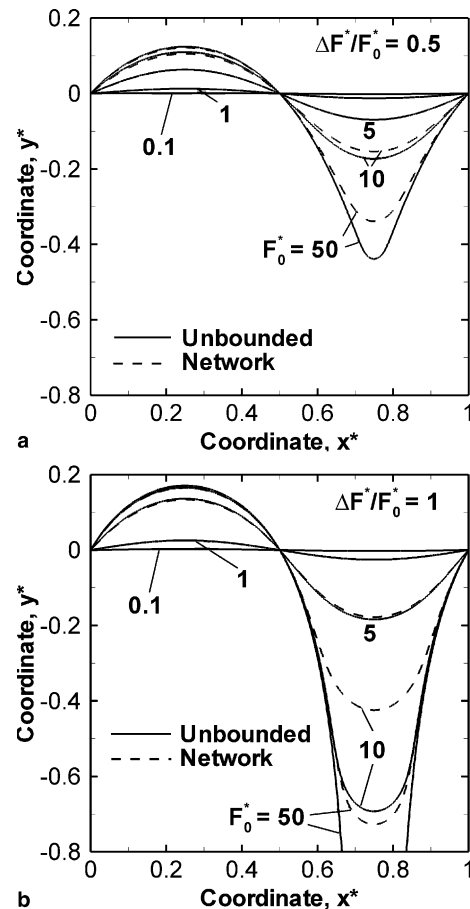

Fig. 4. Steady-state shapes of initially flat boundaries migrating through parallel unbounded dislocation walls (full line), and maximum amplitude shapes (dashed line) for boundaries moving through a dislocation wall network for several mean values, F_0^*, and two relative amplitudes $\Delta F^*/F_0^*$: (a) 0.5 and (b) 1.
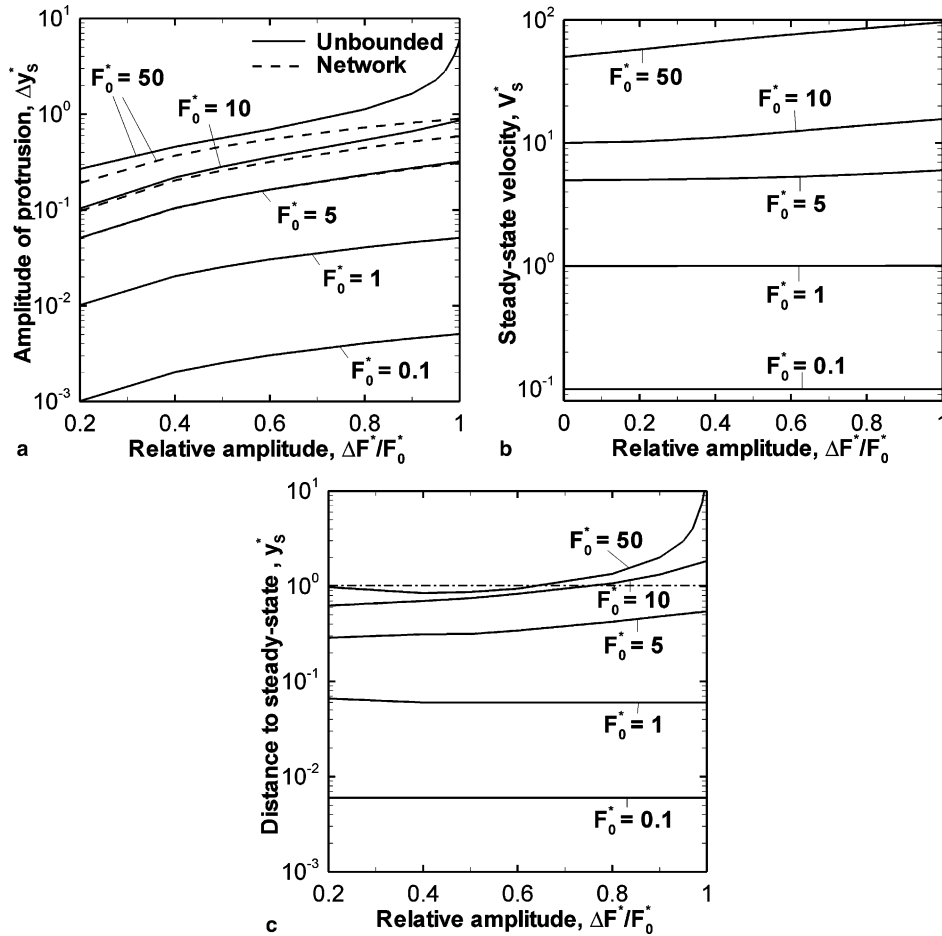
Fig. 5. Effects of mean value F_0^* and relative amplitude $\Delta F^*/F_0^*$ of the sinusoidal driving pressure acting on an initially straight boundary: (a) steady-state amplitude of protrusions for unbounded dislocation walls (full lines) and maximum amplitude for network of dislocations (dashed lines); (b) steady-state velocity for unbounded dislocation walls; (c) distance moved to reach steady state for unbounded dislocation walls.

The variation with F_0^* is more significant, with the amplitude of the protrusions, $\Delta y^* = \Delta y/\lambda$, increasing by orders of magnitude when F_0^* changes from 0.1 to 50 at $\Delta F^*/F_0^* = 1$. Note that $\Delta F^*/F_0^* = \Delta F/F_0$ is independent of the wall separation λ. For a uniform strain energy density difference, $\Delta F^* = 0$, the boundary steady-state velocity is $V_S^* = F_0^*$. This velocity is little dependent on the amplitude, ΔF^*. Generally, the steady-state velocity is virtually unchanged in the presence of protrusions, except for large F_0^*, when the boundaries with larger protrusions move more rapidly and $V_S^* > F_0^*$. Finally, the length y_S^* travelled by the initially straight boundary to reach steady state increases with increasing F_0^* and, again, increases with ΔF^* only for large F_0^* values. This distance is important in the analysis that will be presented below of boundary migration under a network of dislocation walls, because it shows when the boundary may reach steady state within one row of walls.

4.2. Initially straight boundaries: network of dislocation walls

All calculations were made for a symmetrical network with $w = \lambda$ (see Fig. 1(c)). The ends of the dislocation walls

are then at $y^* = 0, 1, 2, \ldots$ with the initially flat boundary at $y^* = 0$. Examples of boundary migration are shown in Fig. 2(b) and (c) for two pairs F_0^*, $\Delta F^*/F_0^*$. As the boundary enters a new row of dislocation walls, the driving pressure F is shifted abruptly in the x^* direction by $\lambda/2$ and the boundary begins to invert its amplitude, which oscillates between a minimum (close to zero) and a maximum.

There are two different situations illustrated in Fig. 2(b) and (c): (i) the boundary reaches steady state while traversing one row of walls (Fig. 2(b)) or (ii) the boundary does not reach steady state within the row (Fig. 2(c)), i.e. were the row width w larger, the boundary amplitude would have continued to increase before entering a new row. To predict either type of behaviour, the results for the dislocation wall network must be compared with those for the unbounded dislocations walls, as given in Fig. 3. In Fig. 3(a), the boundary amplitude for the wall network increases to the steady-state amplitude, which equals the steady-state amplitude for unbounded walls. In this case, the row width is sufficiently large to allow the steady-state shape to be reached. In Fig. 3(b), however, the boundary enters a new row at $y_{(x^*=0)}^* = 1$ before the steady-state amplitude had been reached. Consequently, its maximum

amplitude is smaller than that of the steady state reached with unbounded walls.

From this discussion, it is possible to predict the behaviour of the boundary in a dislocation wall network by analysing its behaviour in the case of unbounded dislocation walls. When the distance travelled by the boundary to reach steady state for unbounded walls outweighs the row width of the wall network, i.e. $y_S^* > 1$, steady state is not reached and the maximum boundary amplitude is smaller than that of the steady state. Otherwise ($y_S^* \leqslant 1$), steady state is reached within each row.

When the boundary faces unbounded walls, the reduced distance to reach steady state, y_S^*, is given as a function of F_0^* and $\Delta F^*/F_0^*$ in Fig. 5(c). Notice that $y_S^* < 1$ when $F_0^* = 5$ and $\Delta F^*/F_0^* = 0.5$, indicating that the boundary in Fig. 2(b) reaches steady state while traversing one row of walls. The maximum amplitude of the protrusions is, in this case, equal to that of the steady state for unbounded walls (Fig. 2(a)). In contrast, $y_S^* > 1$ when $F_0^* = 10$ and $\Delta F^*/F_0^* = 1$, and the boundary does not reach steady state while traversing one row, as can be seen in Fig. 2(c). The maximum amplitude reached is then smaller than that of steady state for unbounded walls. The amplitudes in the two cases (unbounded walls and wall network) are shown in Fig. 5(a) as a function of F_0^* and $\Delta F^*/F_0^*$. For $F_0^* \gtrsim 5$, steady state is never reached for the wall network and the maximum boundary amplitude is smaller than that of the steady state of unbounded walls.

4.3. Initially circular boundaries: unbounded dislocation walls

The evolution of initially circular boundaries subjected to the sinusoidal driving pressure given by Eq. (3) with periodicity defined by $n = 4$ and $n = 40$ is shown in Fig. 6 for $F_0^* = 10$ and $\Delta F^*/F_0^* = 1$. The radial velocity of each point of the boundary becomes constant after some time, but changes from point to point. Therefore, in contrast to the initially flat boundary, the initially circular boundary does not reach steady state (i.e. a time-invariant shape), as shown in Fig. 6(a). It was found, however, that the successive boundary shapes become self-similar at sufficiently long times, i.e. a scaling regime is reached in which the boundary shapes become scaled by a radial coordinate at, say, $\theta = 0$. In terms of the similarity variable $r^*/r^*(\theta = 0, t^*)$ the boundary shape remains invariant (Fig. 6(b)). It was found that, for fixed n, the shapes in the scaling regime depend only on $\Delta F^*/F_0^*$ and not on ΔF^* or F_0^* separately. These scaled shapes are shown in Fig. 7 for various values of $\Delta F^*/F_0^*$ and for $n = 4$ and 40.

As for the initially flat boundary, the curvature at the valleys increases with increasing $\Delta F^*/F_0^*$ and seems to tend to infinity (cusp-like valley). The amplitude of the undulations

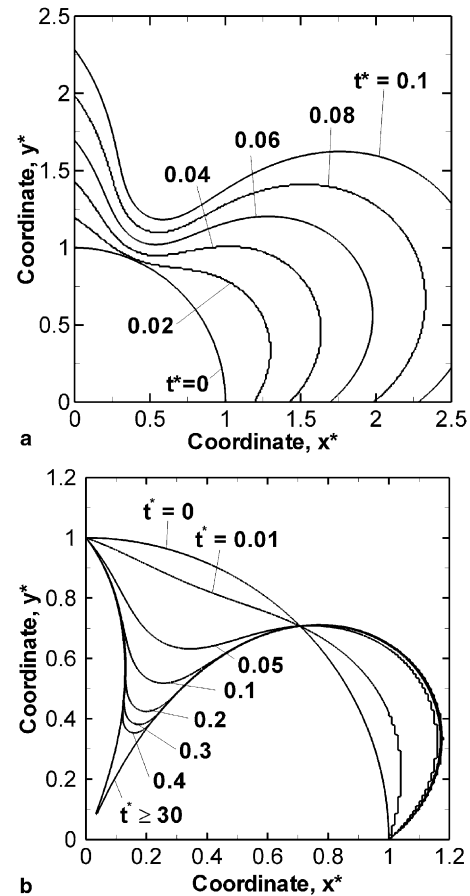$$\frac{\Delta r^*}{r^*(\theta = 0, t^*)} = \frac{r_{max}^* - r_{min}^*}{r^*(\theta = 0, t^*)}$$

Fig. 6. Calculated time evolution of an initially circular boundary for $n = 4$ (angular period $\pi/2$), $F_0^* = 10$ and $\Delta F^*/F_0^* = 1$: (a) not scaled and (b) scaled by the r^* coordinate at $\theta = 0$ (see Fig. 1).

in the scaling regime increases monotonically with increasing $\Delta F^*/F_0^*$ as shown in the plot of Fig. 8 for $n = 4$.

4.4. Comparison with experimental results

A comparison between experiments and the theoretical results obtained in the present work is attempted in this section. However, conclusions must be drawn carefully, since the experimental results of boundary protrusion amplitudes and the estimates of driving pressures are accurate only to an order of magnitude owing to many sources of error. For example, the measured amplitude of protrusions at a grain boundary can be significantly changed by the relative inclination of the observation plane, representing an important source of error. Moreover, the detailed structure of cells/subgrains establishing the driving pressure along the grain boundary is usually not reported when protrusions are observed, allowing only crude estimates of this pressure.

The work of Henshall et al. [21] on the dynamic recrystallization of an Al–5.8 at.% Mg alloy deformed in torsion at 698 K contains sufficient data (specially as regards the subgrain structure) to compare with the present theoretical results. The boundary protrusions shown in the micrograph
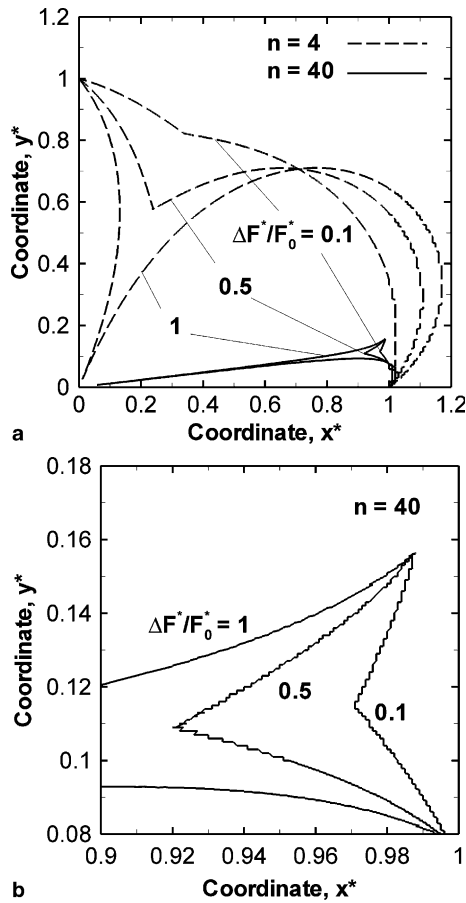
Fig. 7. (a) Boundary shapes in the scaling regime of an initially circular boundary for different relative amplitudes of driving pressure ($\Delta F^*/F_0^*$) and two different angular periods ($2\pi/n$). (b) Magnification of boundaries for $n = 40$ and the same $\Delta F^*/F_0^*$ as in (a).
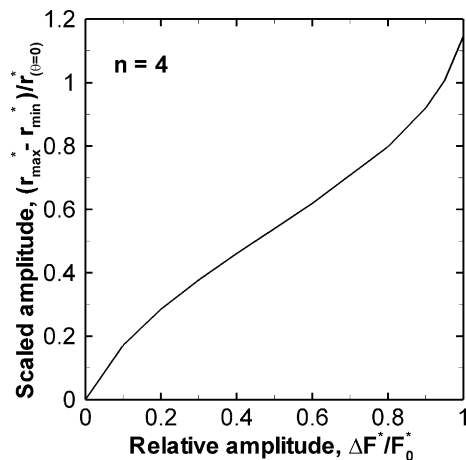

Fig. 8. Scaled amplitude of protrusions in the scaling regime of an initially circular boundary as a function of the relative driving force amplitude for $n = 4$.

of Fig. 6(c) of their work were chosen for the comparison, because protrusions are observed in nearly all grain boundaries and their amplitudes and wavelengths are much smaller than their separation distances. A wide range of

protrusion amplitudes $\Delta y (\sim 10–80 \ \mu m)$ and wavelengths λ ($\sim 100–130 \ \mu m$) can be seen in the field included in the micrograph. This might be an indication of the magnitude of the errors involved in the determination of the protrusion dimensions.

The range of protrusion amplitudes and wavelengths corresponds to $\Delta y^* = \Delta y/\lambda$ in the interval of 0.1–0.6. The driving force originated from the hot-working process used by Henshall et al. [21] is assumed to be mainly the energy stored in the subgrain structure, which, for a strain $\varepsilon \approx 1.1$, has an average size $d_{SGB} \approx 8.8 \ \mu m$. The average measured misorientation across cells/subgrains was $\theta_{SGB} \approx 1.3°$. The energy per unit area of a subgrain boundary of misorientation θ_{SGB} can be calculated from the Read–Schockley equation [22] as

$$\sigma_{SGB} = \sigma \frac{\theta_{SGB}}{15} \left[1 - \ln \left(\frac{\theta_{SGB}}{15} \right) \right] \approx 0.090 \ J/m^2 \quad (9)$$

where the high-angle ($\theta \geqslant 15°$) grain boundary energy $\sigma \approx 0.3 \ J/m^2$ and θ_{SGB} is expressed in degrees. Therefore, the average energy density accumulated in the structure, which equals the average driving pressure F_0, can be estimated as [22] $F_0 = (2/d_{SGB}) \ \sigma_{SGB} \approx 2 \times 10^4 \ J/m^3$. The reduced average driving pressure is $F_0^* = \lambda F_0/\sigma \approx 7$ for $\Delta y^* = 0.1$, and $F_0^* \approx 9$ for $\Delta y^* = 0.6$. Finally, the relative driving force amplitudes, $\Delta F^*/F_0^*$, obtained from Fig. 5(a), are approximately 0.3 and 1, respectively. These are reasonable values, since $\Delta F^*/F_0^* = 1$ is the largest possible relative amplitude and corresponds to the maximum concentration of driving pressure at the peaks, i.e. the formation of sharp subgrain walls, which can indeed be observed in the micrograph of Fig. 3(c) from Henshall et al. [21]. In all, a fair agreement is observed between the results from the present model and those reported by Henshall et al. [21]. However, it is important to remember that the model developed in this paper is a 2D model and that the driving pressure F was assumed sinusoidal, which limits its concentration at the peaks.

5. Concluding remarks

Protrusions at a migrating grain boundary arise when there is a non-uniform strain energy density difference, F, between the two grains separated by the boundary. Protrusions or serrations may also result from anisotropic boundary energy and/or mobility, but these possibilities were not contemplated in this study. In the growth of a recrystallized grain, F (the excess strain energy density in the matrix) is sufficiently large to overcome the surface energy increase of the migrating boundary. This excess energy density was represented by a sinusoidally varying F of mean value F_0, amplitude ΔF, and wavelength λ, dependent on a single space coordinate (y or r, respectively, for initially straight (at $y = 0$) and circular (at $r = r_0$) boundaries). For this simple F, the time evolution of the boundary was obtained by numerical integration of an appropriate form of the classic kinetic equation (Eq. (1)) for the velocity of the boundary

along its normal, used in this paper for the first time. For unbounded dislocation walls it was found that the migrating boundaries reach a steady-state shape or a scaled shape, respectively, for the initially straight and circular boundaries, which were characterized in some detail.

When the boundary moves through the simplified network of dislocation walls shown in Fig. 1(c), the maximum amplitude is the same as that for unbounded walls (steady state is reached) if the reduced length $y_S^* < 1$. When $y_S^* > 1$, a steady state is not reached within a row and the maximum amplitude of the protrusions is smaller than that for unbounded walls.

The high symmetry arrangements of dislocation walls around the recrystallized grain and the simplified representation of their strain energy by a sinusoidal function are, of course, great simplifications of reality: three-dimensional grains, 'random' arrangement of the dislocation walls, complex strain field dependent on more than one space variable. In spite of those simplifications, the model used in this paper highlights the main features of the growth of protrusions in growing recrystallized grains and is in reasonable agreement with experimental results.

Acknowledgements

References

[1] Doherty RD, Hughes DA, Humphreys FJ, Jonas JJ, Jensen DJ, Kassner ME, et al. Mater Sci Eng A Struct 1997;238:219.
[2] Stüwe HP. In: Haessner F, editor. Recrystallization of metallic materials. Stuttgart: Riederer-Verlag; 1978. p. 11. p. 11.
[3] Humphreys FJ, Hatherly M. Recrystallization and related annealing phenomena. Amsterdam/London: Elsevier; 2004.
[4] Kassner ME, Mcmahon ME. Metall Trans A 1987;18:835.
[5] Drury MR, Humphreys FJ. Acta Metall Mater 1986;34:2259.
[6] Beck PA, Sperry PR. J Appl Phys 1950;21:150.
[7] Mcqueen HJ, Ryan ND, Konopleva EV, Xia X. Can Metall Quart 1995;34:219.
[8] Konopleva EV, Mcqueen HJ, Evangelista E. Mater Charact 1995;34:251.
[9] Lens A, Maurice C, Driver JH. Mater Sci Eng A Struct 2005;403:144.
[10] Martin JW, Doherty RD, Cantor B. Stability of microstructure in metallic systems. Cambridge: Cambridge University Press; 1997.
[11] Koul AK, Gessinger GH. Acta Metall Mater 1983;31:1061.
[12] Larson JM, Floreen S. Metall Trans A 1977;8:51.
[13] Henry MF, Yoo YS, Yoon DY, Choi J. Metall Trans A 1993;24:1733.
[14] Hong HU, Nam SW. Mater Sci Eng A Struct 2002;332:255.
[15] Schmidt S, Nielsen SF, Gundlach C, Margulies L, Huang X, Jensen DJ. Science 2004;305:229.
[16] Taylor JE, Cahn JW, Handwerker CA. Acta Metall Mater 1992;40:1443.
[17] Taylor JE. Acta Metall Mater 1992;40:1475.
[18] Kreyszig E. Differential geometry. New York: Dover Publications; 1991.
[19] Gerald CF, Wheatley PO. Applied numerical analysis. Boston (MA): Pearson/Addison-Wesley; 2004.
[20] Martorano MA, Fortes MA, Padilha AF. Model Simul Mater Sci 2006;14:83.
[21] Henshall GA, Kassner ME, Mcqueen HJ. Metall Trans A 1992;23:881.
[22] Radhakrishnan B, Zacharia T. Model Simul Mater Sci 2003;11:307.